coatings

MDPI

Review

Influence of Defects and Heteroatoms on the Chemical Properties of Supported Graphene Layers

Giovanni Carraro [1], Letizia Savio [1] and Luca Vattuone [1,2,*]

[1] IMEM CNR Unità Operativa di Genova, 16121 Genova, Italy; giovanni.carraro@imem.cnr.it (G.C.); letizia.savio@imem.cnr.it (L.S.)
[2] DIFI Università Degli Studi di Genova, 16121 Genova, Italy
* Correspondence: vattuone@fisica.unige.it

Abstract: A large and growing number of theoretical papers report the possible role of defects and heteroatoms on the chemical properties of single-layer graphene. Indeed, they are expected to modify the electronic structure of the graphene film, allow for chemisorption of different species, and enable more effective functionalisation. Therefore, from theoretical studies, we get the suggestion that single and double vacancies, Stone–Wales defects and heteroatoms are suitable candidates to turn nearly chemically inert graphene into an active player in chemistry, catalysis, and sensoristics. Despite these encouraging premises, experimental proofs of an enhanced reactivity of defected/doped graphene are limited because experimental studies addressing adsorption on well-defined defects and heteroatoms in graphene layers are much less abundant than theoretical ones. In this paper, we review the state of the art of experimental findings on adsorption on graphene defects and heteroatoms, covering different topics such as the role of vacancies on adsorption of oxygen and carbon monoxide, the effect of the presence of N heteroatoms on adsorption and intercalation underneath graphene monolayers, and the role of defects in covalent functionalisation and defect-induced gas adsorption on graphene transistors.

Keywords: graphene; adsorption; defect; heteroatoms

Citation: Carraro, G.; Savio, L.; Vattuone, L. Influence of Defects and Heteroatoms on the Chemical Properties of Supported Graphene Layers. *Coatings* **2022**, *12*, 397. https://doi.org/10.3390/coatings12030397

Academic Editor: Vera Marinova

Received: 24 January 2022
Accepted: 15 March 2022
Published: 17 March 2022

1. Introduction

The possibility of using graphene-based materials as "metal-free" catalysts [1,2] is attracting enormous interest, since it reduces the need for precious or rare elements currently used in heterogeneous catalysis. However, ideal and perfect graphene is known to be "perfectly inert", while it is now well established that there is an essential role of defects and dopants in activating its chemical properties.

We mention that graphene defects are generally classified as intrinsic and extrinsic. The former includes structural defects (vacancies, carbon adatoms, Stone–Wales defects, grain boundaries), while the latter results from the introduction of heteroatoms, often leading to doping of the layer. Intrinsic defects are prone to be active sites for the insertion of foreign atoms to form extrinsic defects due to the strain energy in the C–C bonds involved. Therefore, the term "defect" will refer generically to both categories, while the specific kinds of defects will be specified whenever necessary.

Various types of intrinsic defects may be present in graphene layers, such as point defects, large vacancies, line defects, and Stone–Wales. Their presence alters the perfect pi-conjugated electronic structure of the C-lattice and hence exposes reactive carbon atoms. Indeed, in some cases, STM images showed an enhanced local density of states at the defects [1]. They are thus responsible for the chemical properties of graphene. Atomic-scale defects were initially considered random imperfections, but nowadays the improved performance of last-generation high-resolution microscopies allows a realistic view of the different types of defects. e.g., Figure 1 shows some typical metastable defects commonly appearing in the graphene network.

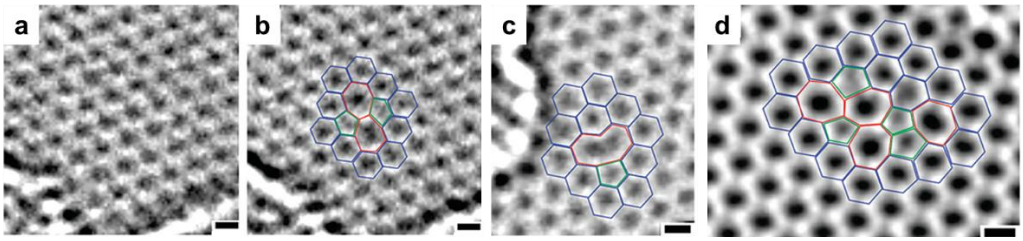

Figure 1. HRTEM images show different kinds of defects in graphene sheets. (**a**) Unperturbed lattice. (**b**) Stone–Wales (SW) defect with atomic configuration superimposed. This topological defect involves the rotation of carbon–carbon (C–C) bonds by $\pi/2$ causing the transformation of four hexagons into two heptagon–pentagon pairs). (**c**) Reconstructed vacancy with the atomic configuration; a pentagon is indicated in green. (**d**) Defect image and configuration comprising four pentagons (green) and heptagons (red). The scale bar corresponds to 2 Å. Taken with permission and adapted from [2]. Copyright by ACS.

An increasing number of recent theoretical papers suggest the possible role of graphene vacancies [3], divacancies [4], Stone–Wales defects [5] and heteroatoms [6,7] in the chemical properties of single-layer graphene (SLG). Indeed, they are expected to modify its electronic structure and to allow for chemisorption of atoms [3] and simple molecules [4] (e.g., hydrogen [8], oxygen [5], CO and CO_2 [9]) and for a more efficient functionalisation [10], thus turning nearly chemically inert graphene into an active player in chemistry, catalysis and sensoristics [11,12].

An overview of the calculated adsorption energy of the different elements at single vacancies of freestanding graphene is shown in Figure 2. The adsorption energies are relatively high for all the elements, with the only exception being noble gases.

H -3.41																He -0.02
Li -2.59	Be -6.29										B -11.76	C -15.60	N -9.51	O -5.41	F -2.43	Ne -0.04
Na -1.74	Mg -1.40										Al -4.75	Si -7.62	P -7.70	S -6.08	Cl -2.51	A -0.08
K -1.92	Ca -2.78	Sc -5.89	Ti -7.22	V -6.87	Cr -5.95	Mn -5.56	Fe -6.32	Ni -5.72	Cu -2.89	Zn -0.30	Ga -3.08	Ge -5.59	As -6.04	Se -4.61	Br -1.89	Kr -0.13
Rb -1.88	Sr -2.39	Y -5.57	Zr -7.51	Nb -7.74	Mo -6.93	Tc -7.31	Ru -7.67	Pd -4.30	Ag 1.28	Cd -0.19	In -1.94	Sn -3.96	Sb -4.72	Te -3.41	I -1.44	Xe -0.11
Cs -2.01	Ba -2.90	La -5.98	Hf -7.64	Ta -7.92	W -8.00	Re -7.31	Os -8.03	Pt -6.02	Au -1.80	Hg -0.19	Ti -1.96	Pb -3.10	Bi -3.83	Po -2.56	At -1.22	Rn -0.15

Figure 2. Adsorption energy (in eV/atom) for atoms at single vacancies of graphene calculated using WdW—DF2. Data were taken from Ref. [3].

Similarly, at divacancies, strong adsorption is expected for O_2, N_2, B_2, and CO molecules, for which adsorption energies of −8.44 eV, −4.53 eV, −13.83 eV, and −3.86 eV, respectively, are predicted [4].

These studies prove that unsaturated C bonds at single and double vacancies are potentially reactive sites for the adsorption of atoms and the chemisorption and possible dissociation of molecules. However, theoretical studies often consider freestanding unsupported graphene, or neglect the interaction between the vacancy and the substrate. Such an oversimplification can, unfortunately, lead to wrong predictions since the role of the substrate must be taken into account in the description of the whole system.

A paradigmatic example in this respect is offered by comparing the reactivity of single graphene vacancies (VG) towards water for G/Cu(111) and G/Pt(111) [13] (Figure 3). In both cases, the dangling C bond initially saturates towards the metal substrate. On

G/Cu(111), water can break this C−Cu bond by dissociating at the under-coordinated carbon atom of the vacancy. Both partial and complete dissociation are exothermic, with calculated energies of −0.38 eV/molecule and −1.54 eV/molecule, respectively. A different behaviour is predicted for the stronger Pt–C bond, for which dissociation energies of +0.69 eV/molecule and −0.16 eV/molecule are predicted for the first and second O–H bond breaking. Therefore, according to the theoretical prediction, water splitting should occur effectively only at G/Cu(111) vacancies.

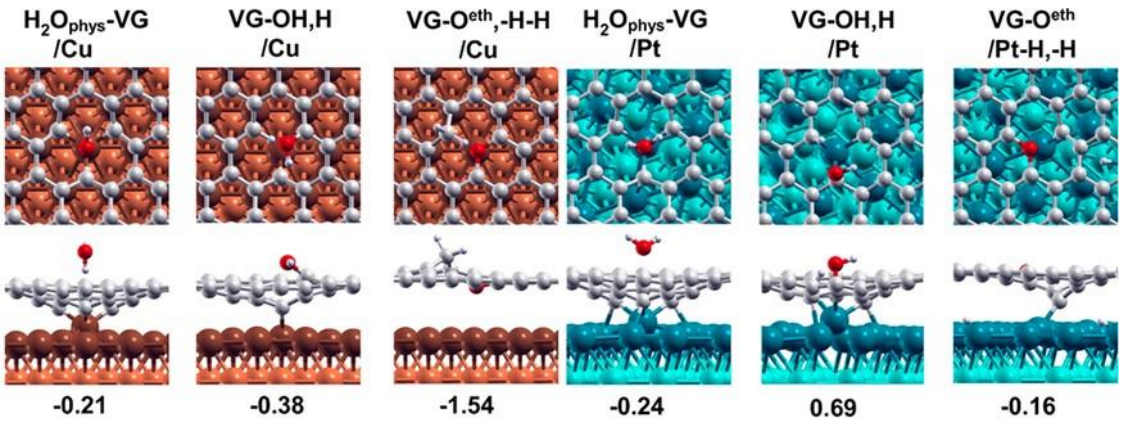

Figure 3. Most stable products along the dissociation path of H_2O for (orange, left) VG/Cu and (light blue, right) VG/Pt interfaces. From left to right: physisorbed state, first dissociation (−OH/−H), and complete dissociation (−O/−H/−H). Taken with permission and adapted from Ref. [13]. Copyright by ACS.

In general, it is also not trivial to determine whether adsorption occurs at the vacancy above the graphene layer or at the interface between it and the substrate. The outcome depends on the relative strength of the C-substrate, C–molecule/fragment and substrate-molecule/fragment bonds and on the energetic cost of intercalation, which can be relevant when graphene is strongly interacting with the substrate. e.g., Figure 4 compares the result of ab initio calculation for the dissociation of water at graphene vacancies of freestanding graphene (upper row) or of a G layer supported on TiO_2. In the latter case, the water molecule may be above the vacancy (medium row) or at the VG/TiO_2 interface (lower row). In the presence of vacancies, it is apparent that the dissociation of water is mainly exothermic, both at the graphene layer (by −4.32 eV/molecule) and at the interface (by −4.29 eV/molecule), so that both processes are permitted from the thermodynamic point of view.

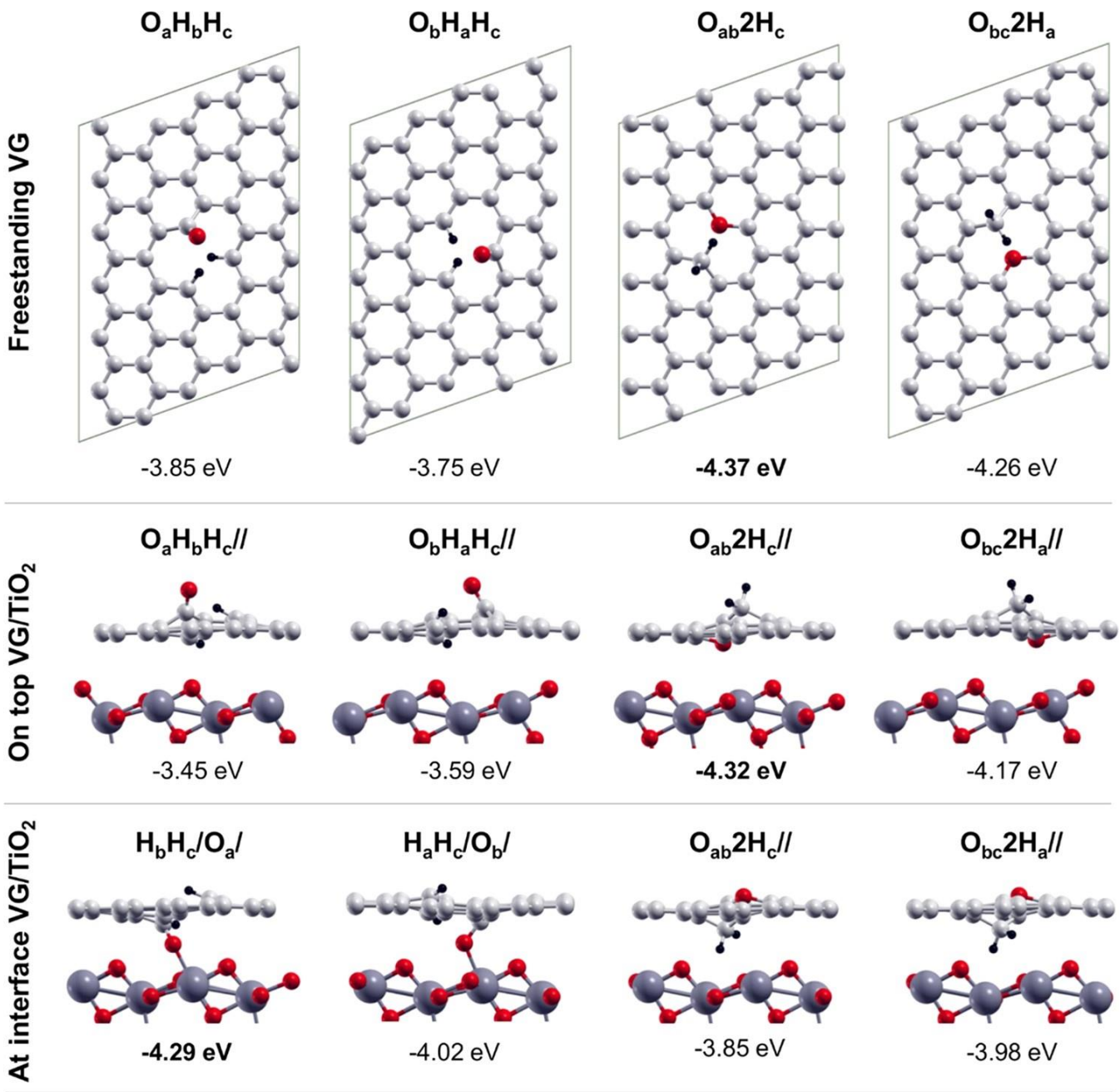

Figure 4. Top views of the fully dissociated products of water on freestanding VG (top line); side views of the fully dissociated products of water (O + H + H) on top of VG/TiO2 (middle line), and at the interfaces of VG/TiO_2 (bottom line). Small red, light grey, and black balls represent O, C, and H atoms, respectively. Big dark grey balls represent Ti atoms. Taken with permission from Ref. [14]. Copyright by ACS.

Despite a large amount of theoretical data, only a relatively low number of experimental studies investigated the adsorption of simple molecules at graphene defects. The reason for this lies in the experimental difficulties to obtain a well-defined majority defect.

For example, low energy ion bombardment is a widely available tool to produce defects in single-layer graphene, but different kinds of defects can be generated depending on the mass, energy, and angle of incidence of the ion.

The simulation of the effect of impact of an inert gas ion on graphene is reported in Figure 5, which shows low ion energy should be used to produce mainly single vacancies,

but that production of some double vacancies cannot be excluded. This prediction is confirmed experimentally in the case of G/Pt(111): upon bombardment with 140 eV Ar^+ ions, a majority of single vacancies [15] and also divacancies [16] are produced. With increasing energy, more complex defects are produced and significant damage to the substrate must also be taken into account. e.g., H+ and N+ implantation into 6H–SiC (0001) was observed using 100 keV ions [17].

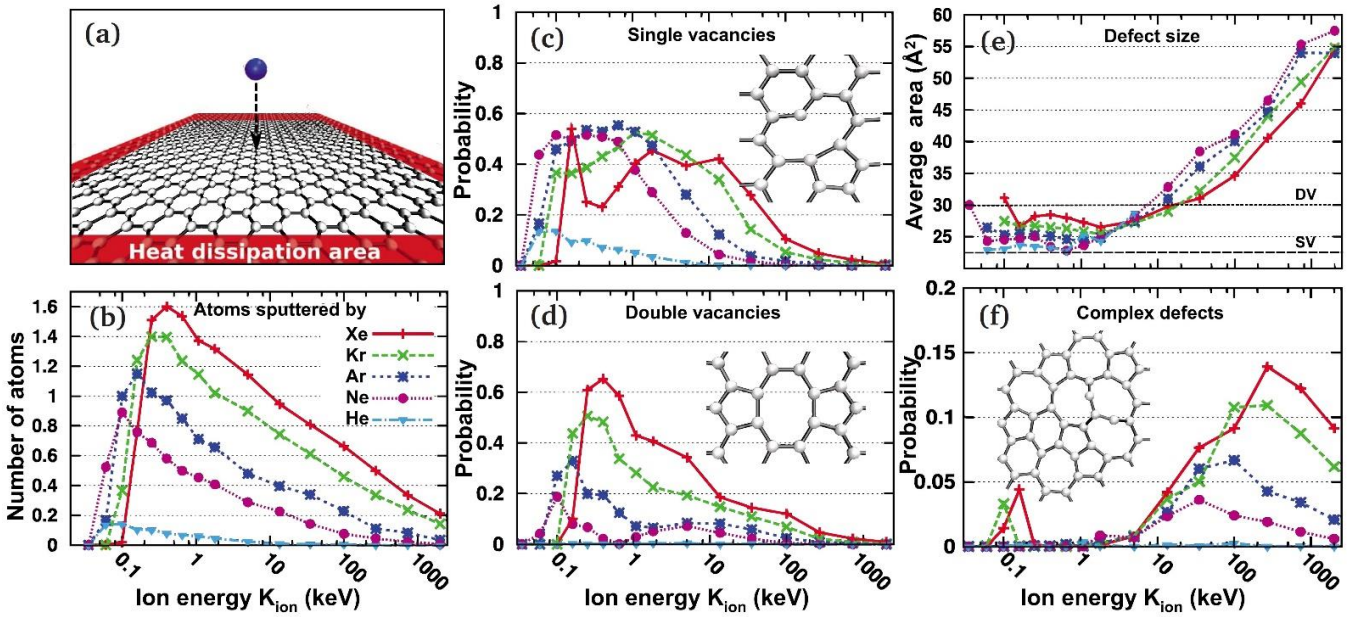

Figure 5. Production of defects in graphene under ion irradiation as revealed by the analytical potential molecular dynamics. (**a**) Simulation setup. (**b**) The number of sputtered atoms per ion impact as a function of ion energy. (**c**,**d**) Probability for single and double vacancy formation as a function of ion energy. The insets show the atomic structures of the reconstructed vacancies. (**e**) Average area covered by a single defect (when formed)—typically still an sp^2-bonded network of carbon atoms. The areas corresponding to an SV and DV are marked. (**f**) Probability for creating defects other than SV/DV. Taken with permission from Ref. [18]. Copyright by APS.

In this paper, we review experimental findings about adsorption on graphene point defects (Section 2) and heteroatoms (Section 3). We cover different topics such as the role of vacancies on adsorption and intercalation of simple gas molecules as oxygen [19] and carbon monoxide [20], the effect of the presence of N heteroatoms on the adsorption properties of graphene [21,22] and the role of defects in covalent functionalisation [23]. In Section 4, we mention some more applicative examples, such as the operation of a transistor based on gas adsorption on defects [24] and the possible use of graphene doped with heteroatoms for gas sensing.

2. Reactivity at Graphene Vacancies

Structural defects can be introduced in graphene, during or after the growth, by ion or electron bombardment of the G layer or by chemical oxidation [25]. An intrinsic difficulty when studying how structural defects affect graphene's electronic and chemical properties is to determine if a majority defect has been produced and to identify and quantify it. For example, Costa et al. [26] probed experimentally the influence of the defect concentration on the fluorination reaction of mono and bilayer graphene supported on SiO_2/Si. Defects were induced by plasma treatment and quantified by Raman spectroscopy, but the authors admit that their nature is not well defined and that "the defects prepared by oxygen plasma represent "typical" defects found in typical graphene samples." They conclude that the fluorination rate is poorly affected by the concentration of defects for SLG, while for the

bilayer, a lower degree of fluorination is observed at low defect concentration, which increases for the more defective samples. The presence of two competitive mechanisms rationalises the observed results as follows: on one side, defects make graphene more reactive, on the other side the reactivity of specific defects also plays a role.

The influence of defects produced by Ar^+ plasma on the chemical functionalisation of single-layer G was also investigated by Xiao-Liang et al. [10], who developed a geometrical model to correlate the defects density (n_d) to the adsorption of aryl radicals on the surface. The exact n_d value of each SLG was determined from the intensity ratio of the D and G bands in Raman spectra. Functionalisation of these layers was then performed via diazonium salt-promoted radical addition reactions from solution [27,28]. The presence of covalently grafted pyridinyl groups was proved by correlating the number of defects with the intensity of specific N 1s and C 1s peaks at 400.0 eV and 286.1 eV, respectively, assigned to the pyridinyl group and sp^3-hybridised carbon. This behaviour confirms that the presence of the defects can enhance the reactivity of SLG toward chemical functionalisation.

Theoretical calculations [13,29] and vibrational spectroscopy [30] have demonstrated that water can dissociate at defect sites on graphene, forming C−H and C−OH bonds. Feng et al. [31] investigated the effect of water, oxygen, hydrogen, and ammonia adsorbing and reacting on G/Ru(0001) and G/Cu(111) by STM. On Ru(0001), water easily attacks the line defects of graphene and splits it into multiple fragments already at 90 K, opening a pathway for water intercalation. On Cu(111), the effect of water is milder, indicating that there is a strong influence of the substrate chemical nature on reactivity of the C–C bonds in epitaxial graphene. Surprisingly, the other molecules investigated did not show such effects.

While the studies mentioned so far did not focus on a punctual and specific defect, some efforts have been made to produce surfaces with a well-defined, majority defect, the simplest of which is the single vacancy produced by sputtering, as mentioned above [18].

Li et al. [19] investigated the reactivity of graphene vacancies on Ru(0001) by low energy ion scattering (LEIS). Vacancies were created by low energy (around 50 eV) Ar^+ bombardment. The sample was then exposed to O_2 at room temperature (RT). Figure 6 compares LEIS spectra recorded after dosing O_2 on pristine G/Ru(0001) (a) and on G after mild sputtering of the surface for 3 min (b). The new peak appearing at 2580 eV corresponds to the oxygen single scattering peak (SSP), while the area of the carbon peak does not change. Such a spectrum indicates that randomly distributed single vacancies are present at the surface of graphene and that adsorbed oxygen sits on or near the defect. Subsequent annealing to 600 K for ten minutes (spectrum c) causes the disappearance of the oxygen peak and the increase of the Ru signal. This indicates that oxygen either desorbs or diffuses underneath, reducing the shadowing effects on the Ru sites near the G vacancy.

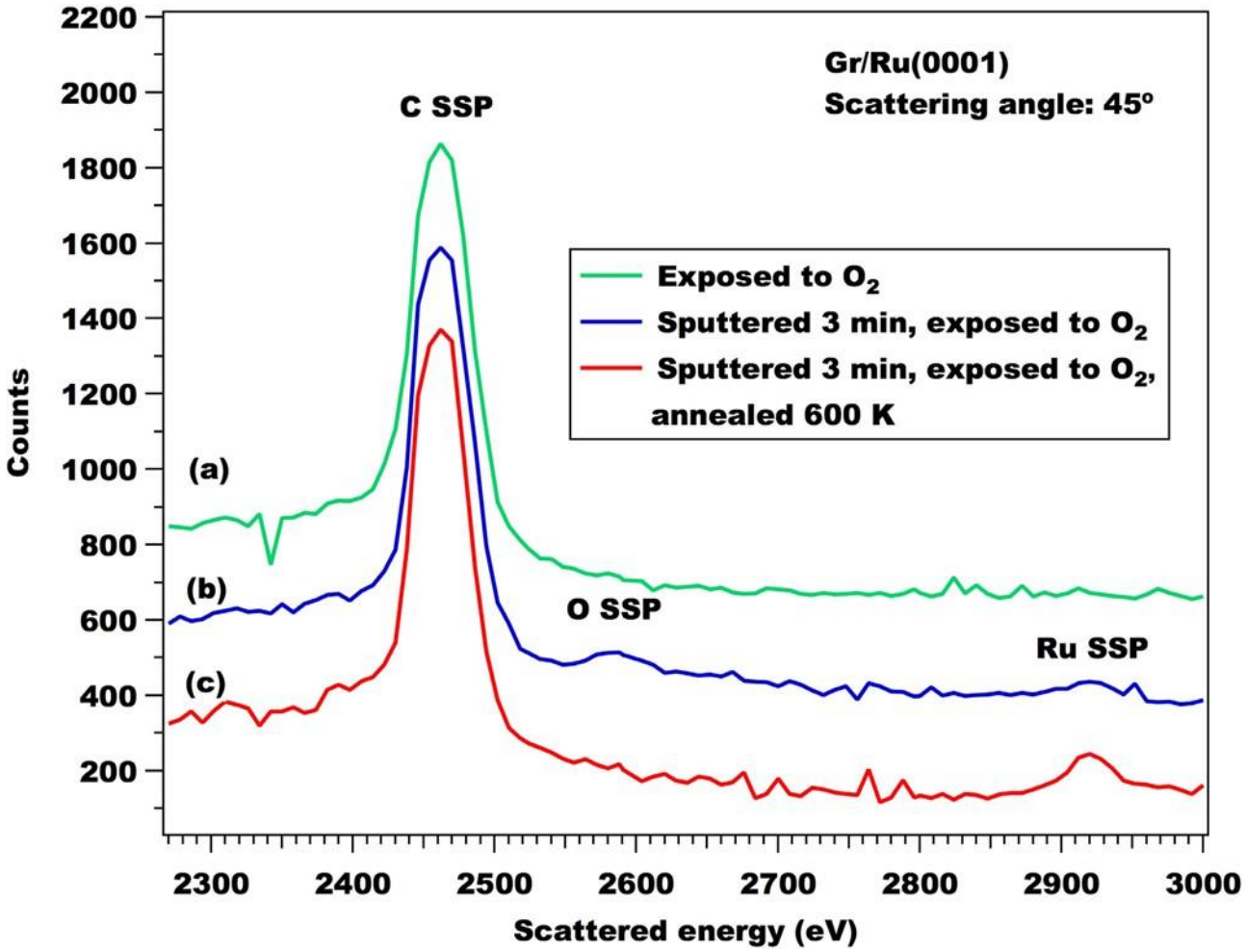

Figure 6. 3000 eV He^+ LEIS spectra collected at a scattering angle of 45° from (a) as-prepared Gr/Ru(0001) exposed to 8000 L of O_2 at 300 K, (b) Gr/Ru(0001) pre-sputtered for 3 min and then exposed to 1500 L of O_2 at 300 K, and (c) after annealing spectrum (b) to 600 K for 10 min. Taken with permission from [19]. Copyright by Elsevier.

The identification of the adsorption site for the ad-molecules is, in general, not trivial; it is indeed difficult to determine whether adsorption takes place at the vacancy or on the underlying substrate. In the case of CO adsorption on G/Ni(111), another system characterised by strong interaction with the substrate, it was possible to conclude that the molecule adsorbs below the vacancy site based on vibrational analysis. Figure 7 shows HREEL spectra (red) recorded after dosing CO on G/Ni(111) (A) and on $G/Cu_{polycrystalline}$ (B) [20]. For each system, the figure compares the spectra recorded on the pristine and on the defected sample (indicated as G*). Mainly single vacancies were produced by 150 eV Ne^+ sputtering. CO exposure at RT causes the presence of additional peaks at 52 meV, 237 meV and 253 meV on the defected G*/Ni(111). Such losses are ascribed to the molecule–surface vibration and to the internal C–O stretch mode for CO at bridge and atop sites, respectively, and they are compatible with those reported for CO adsorbed on Ni(111). Notably, they do not show up for G*/Cu, even after exposure to CO at 90 K, thus ruling out that the lack of CO related features at RT is due to lower adsorption energy. It has to be ascribed to a real inertness of the surface.

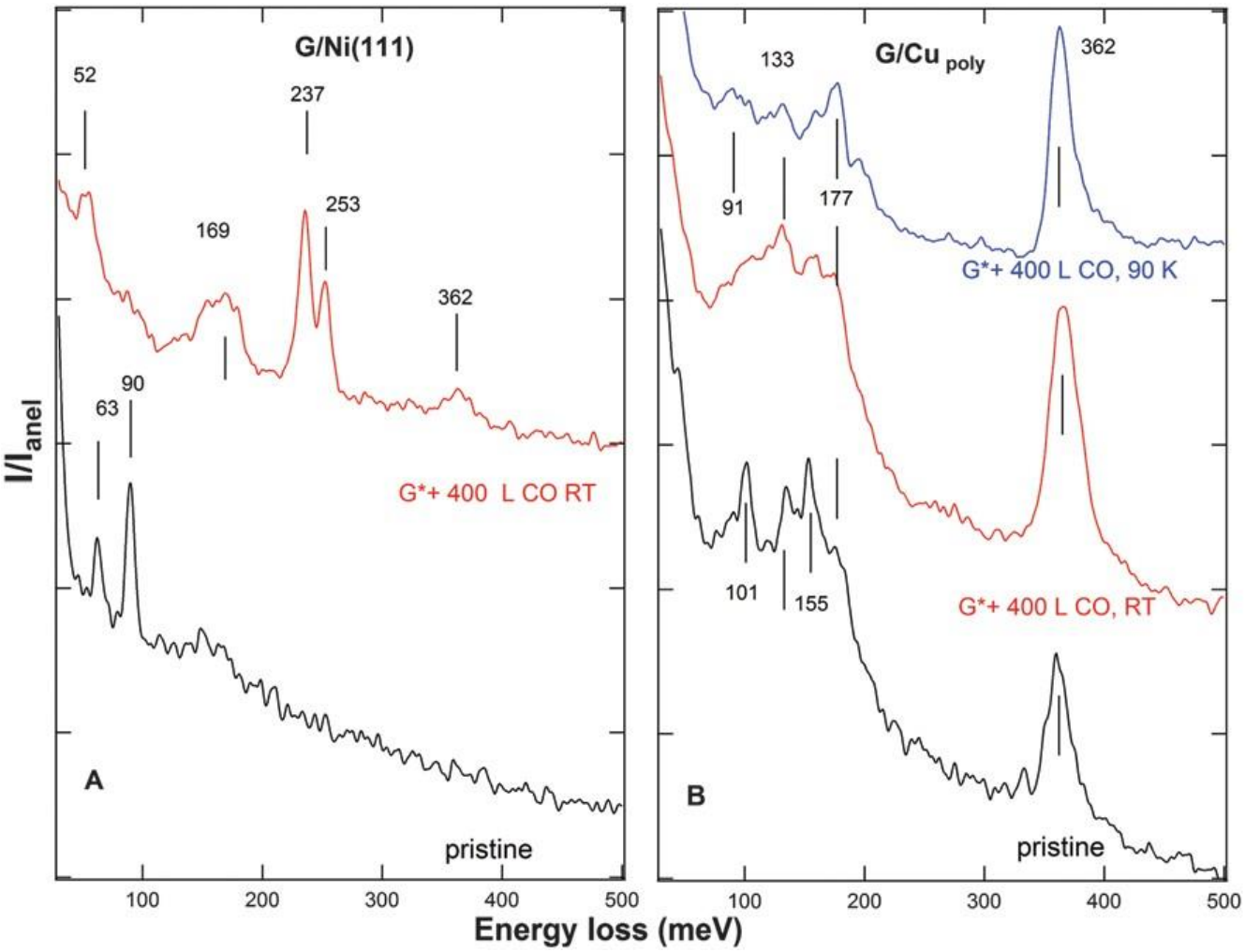

Figure 7. HREEL spectra of G/Ni(111) (panel (**A**)) and G/$Cu_{polycrystalline}$ (panel (**B**)). The bottom traces (black) refer to the pristine samples, the top ones to the layer after sputtering (χ_{Ne+} = 3.2 × 10^{14} Ne^+/cm^2) and exposure to 400 L of CO at RT (red, (**A**,**B**)) ad at 90 K (blue, (**B**) only). Taken with permission from Ref. [20]. Copyright by the Royal Society of Chemistry.

Therefore, this result indicates that CO ad-molecules are not just adsorbed at the vacancy but that the presence of the vacancy enables them to chemisorb on the reactive Ni(111) substrate. If the vacancy itself were reactive, adsorption would take place also for G*/Cu, contrary to experimental evidence.

This conclusion is supported by a recent combined experimental and theoretical study demonstrating the occurrence of CO intercalation through vacancies following exposure in the mbar pressure range; in this case the process is more efficient if the G layer is doped with N atoms [29]. Almost in parallel, in-operando experiments revealed that intercalated CO reacts undercover to produce CO_2 via the Boudouard reaction [32].

Artificially created defects can be used for functionalisation. Besides the example of functionalisation with aryl radicals mentioned above [10], we mention that C vacancies produced by low energy Ar^+ bombardment on G/SiC(0001) can adsorb p-aminophenol (p-AP), a model molecule with an aromatic ring and two different ending groups (see Figure 8a–c for STM images and Figure 8d–f for the corresponding models) [23]. The change in the line scan profile across the vacancy upon absorption is shown in Figure 8g, while Figure 8h reports the XPS spectrum of the N 1s region recorded after exposure to p-AP. The presence of a peak at 399.5 eV on the defected layer demonstrates p-AP adsorption through its nitrogen atom in a substitutional site of the graphene network. Even if pure N

in a graphitic network is expected at 400.5 eV [33], it remains bonded to the p-AP molecule in an sp^3 configuration, causing a decrease in the binding energy.

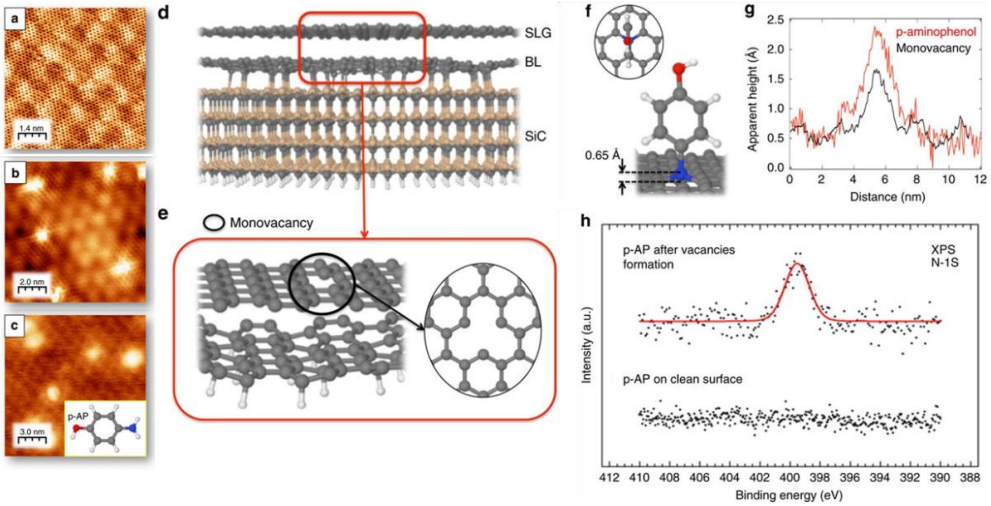

Figure 8. (**a**) Atomically resolved STM image of the (6 3 × 6 √3)R30° reconstruction of the single-layer epitaxial graphene grown on SiC(0001) (I = 0.36 nA, V = −510.9 mV). (**b**) STM image of single-atom vacancies formed upon Ar^+ irradiation on the surface. (I = 2 nA, V = −289mV) (**c**) STM image obtained after exposing defected layer to 4L of p-AP (I = 0.09 nA, V = −1240 mV). (**d**) Pictorial representation of a fully relaxed model of 4H-SiC(0001) SLG/(6√3 × 6√3)R30° unit cell. (**e**) The optimised model's top and side views for a single vacancy created within a SLG on a graphene buffer layer. In this model, the anchoring points between the graphene buffer layer and the SiC(0001) are saturated with H atoms with respect to the model shown in (**d**). (**f**) Top and side views of the optimised geometry of a doubly dehydrogenated p-AP molecule with the nitrogen atom integrated into the SLG lattice within a single vacancy. Average perpendicular to the surface distance between the nitrogen atom and the SLG is also shown. (**g**) Typical STM Profiles on images (**b**,**c**), along with a single-atom vacancy and a p-AP anchored molecule, respectively; (**h**) N 1s core-level spectra after dosing p-AP on an SLG surface without and with atomic vacancies. The N 1s binding energy corresponds to a C atom substitutional in the graphene network. Caption and figure were taken with permission and adapted from [23]—copyright by Springer Nature.

This result is quite relevant for sensoristic applications because the functionalisation with p-AP has a negligible influence on the excellent electronic properties of epitaxial graphene over macroscopic extensions, allowing for the use of p-AP as a linker for more complex molecules [23,34].

3. Reactivity in the Presence of Heteroatoms

An effective method to influence the chemical reactivity of graphene consists of the controlled introduction of foreign atoms (heteroatoms) in the carbon lattice. This chemical doping method has the advantage of forming highly stable compounds, as the heteroatoms bind covalently to the graphene. It is also quite efficient, as a low doping concentration is sufficient to dramatically influence the properties of graphene.

Though a detailed description of the doping methods is beyond the scope of the present document, we mention that, recently, the following methods were developed to produce doped graphene layers: low energy ion implantation [35], CVD [36], thermal annealing [37], arc discharge [38], plasma treatment [39,40], solvothermal [41] and hydrothermal [42,43] methods. Strategies were also developed to obtain materials with mono-dopants [44] or co-dopants [45–48].

The most common non-metallic elements used as heteroatoms are those of the III (B) and V (N, P) groups [49], though some papers reporting about doping with S also appeared in the literature. N-doped samples are probably the most investigated samples.

Figure 9 compares the reactivity of a single layer of G/Ni(111) pristine or doped with N heteroatoms introduced in the layer by low energy N_2^+ bombardment. HREEL spectra, recorded after exposing CO on the pristine sample at 87 K under controlled UHV conditions, show losses at 48 meV, 97 meV, and 260 meV (Figure 9a, bottom trace). They were assigned to the CO-graphene stretch, to some water contamination and to the internal CO stretch, respectively. In the presence of N heteroatoms, no CO adsorption is detected at RT under UHV conditions (Figure 9a, red, middle trace), while an additional feature appears at 237 meV after exposure at 87 K (Figure 9a, top traces) [21]. Therefore, we can identify the 256 meV and 237 meV losses with CO molecules adsorbed at regular graphene sites or at/close to the heteroatoms, respectively. The thermal evolution of the CO-stretch region is reported in panels b and c. It is clear that the 256 meV species desorbs at a lower temperature than the one related to N-doped sites. Therefore, there is no doubt that the presence of N causes the appearance of a more strongly bound CO moiety [50]. Assuming a pre-factor value for desorption of 10^{13} Hz, the adsorption energy in the low coverage limit was estimated to be ~0.85 eV and ~0.54 eV for N-doped and regular graphene sites, respectively.

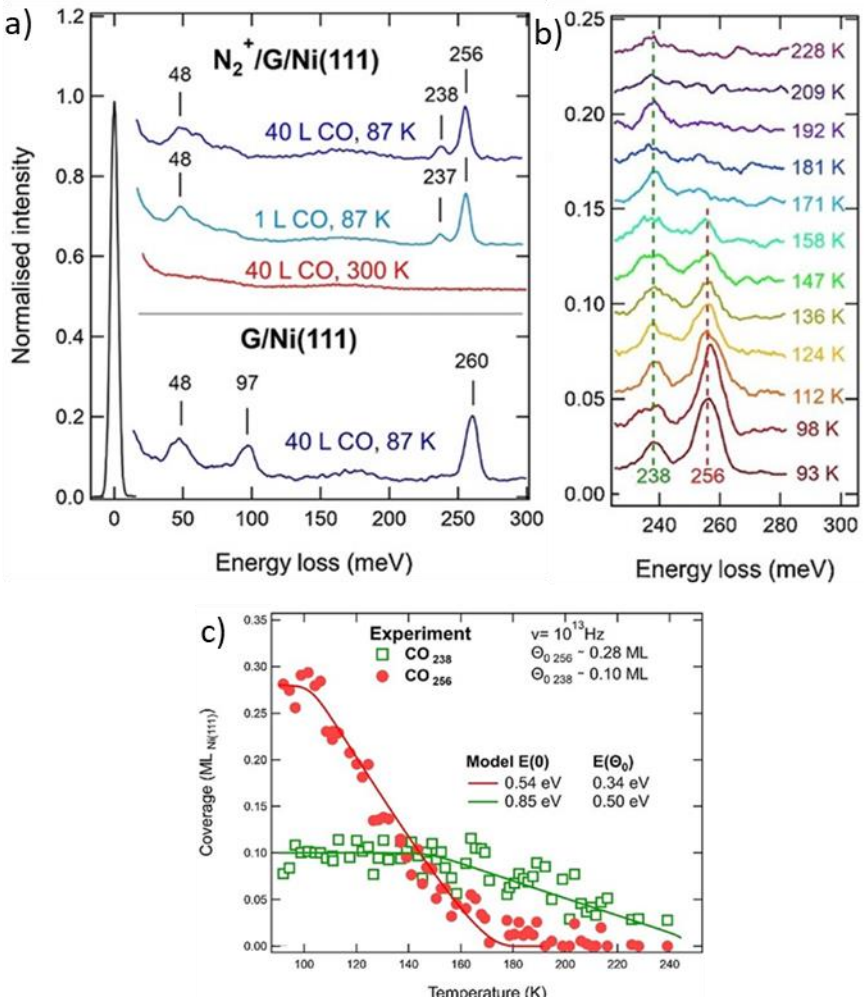

Figure 9. (**a**): HREEL spectra recorded in specular after dosing CO on pristine graphene on Ni(111) at 87 K (blue, lower spectrum), N-doped G/Ni(111) at RT (red, middle trace), N-doped G/Ni(111) at 87 K (blue, top traces). (**b**): Thermal evolution of the HREEL spectra of the N-doped graphene after exposure to CO at 87 K. (**c**): Intensity of the 234 meV and 256 meV peaks vs. annealing temperature. Taken with permission from Ref. [21]. Copyright by Elsevier.

N-doped graphene has been proposed as a candidate metal-free catalyst for the oxygen reduction reaction (ORR).

Lai et al. [51] described how to produce nitrogen-doped graphene either by annealing graphene oxide (G-O) under ammonia or by annealing an N-containing polymer/reduced graphene oxide (RG-O) composite (polyaniline/RG-O or polypyrrole/RG-O). They also demonstrated that such metal-free catalysts could be used for ORR. By comparing cyclovoltammetry measurements performed on different electrodes, the authors investigated the effects of the N precursors and annealing temperature on the catalyst's performance. Their findings show a strong dependence on the selectivity and catalytic activity for ORR, depending on the bonding state of the N atoms. The graphitic N directly affected the reactivity by determining the current density, while the pyridinic N improved the onset potential for ORR [51]. However, the total N content in the graphene-based non-precious metal catalyst does not play an essential role in the efficiency of the ORR process.

Jiao et al. [52] compared the activity of graphene doped with different heteroatoms towards ORR. In Figure 10a–f, we report the XPS spectra of the main line of the dopants, while Figure 10g shows a "volcano"-like plot correlating the theoretically expected current j_0^{theory} to ΔG_{OOH^*}.

The ORR reaction can be written as:

$$O_2 + 2H_2O + 4e^- \rightarrow 4OH^- \quad (1)$$

Moreover, it can follow one associative and two dissociative reaction pathways. However, since the surface of doped graphene presents a relatively high energy barrier (>1.2 eV) in the dissociative pathway, the associative mechanism below:

$$O_2(g) + 2\,H_2O(l) + 4e^- + * \rightarrow OOH^* + OH^- + H_2O(l) + 3\,e^- \rightarrow O^* + 2\,OH^- + H_2O(l) + 2e^- \rightarrow OH^* + 3OH^- + e^- \rightarrow 4OH \quad (2)$$

is dominant, and was considered in their calculations to estimate ΔG_{OOH^*}.

ΔG_{OOH^*} is the free energy change between the initial state and the one showing the OOH* intermediate. For each synthesised sample, j_0^{expt} (blue squares) closely follows the trend predicted in the plot. Moreover, due to the weak binding of OOH* on graphene-based surfaces, the calculated points are all on the right branch of the volcano plot. An optimal catalyst should have a higher current density j_0, corresponding to a ΔG_{OOH^*} closer to the centre of the volcano-like plot. The "ideal" X-graphene should be at the summit of the volcano, with a calculated value of 2.12×10^{-6} A/cm^2, i.e., ~5 times higher than that of Pt/C catalyst under the same testing conditions.

N-doped graphene, together with MoS_2, was demonstrated to have also photocatalytic activity resulting in the degradation of ammonia under near-infrared irradiation, a frequency range corresponding to about 54% of the solar spectrum. The activity of this new catalyst (99.6%) is significantly higher than the one (64%) attainable using only MoS_2 and extremely stable since it is still as high as 90.7% after five runs [53].

Guo et al. [54] investigated the active site for ORR in N-doped G by preparing HOPG model catalysts with well-defined N-doping. They observed that the ORR reactivity linearly correlates with the pyridinic N concentration. From comparing pre- and post-ORR XPS spectra and from the analysis of the TPD results for the model HOPG exposed to CO_2 at RT, they deduced that the active site is not the pyridinic N itself but, more precisely, a Lewis base site created in the carbon atoms neighbouring the N atom.

Finally, we mention that the presence of heteroatoms such as N may affect also the magnetic properties of the graphene layer. As an example, we cite the case of N-doped graphene (N content: 9.8%) produced by treating fluorographene with hydroxylamine (NH_2OH) at 130 °C in dimethylformamide (DMF). Such treatment avoids high-temperature or the use of highly reactive reagents. This material features both localised spin centres and spin-containing sites with itinerant electron properties and exhibits a spin-switch behaviour (on–off–on) controlled by microwave irradiation at X-band frequency [55].

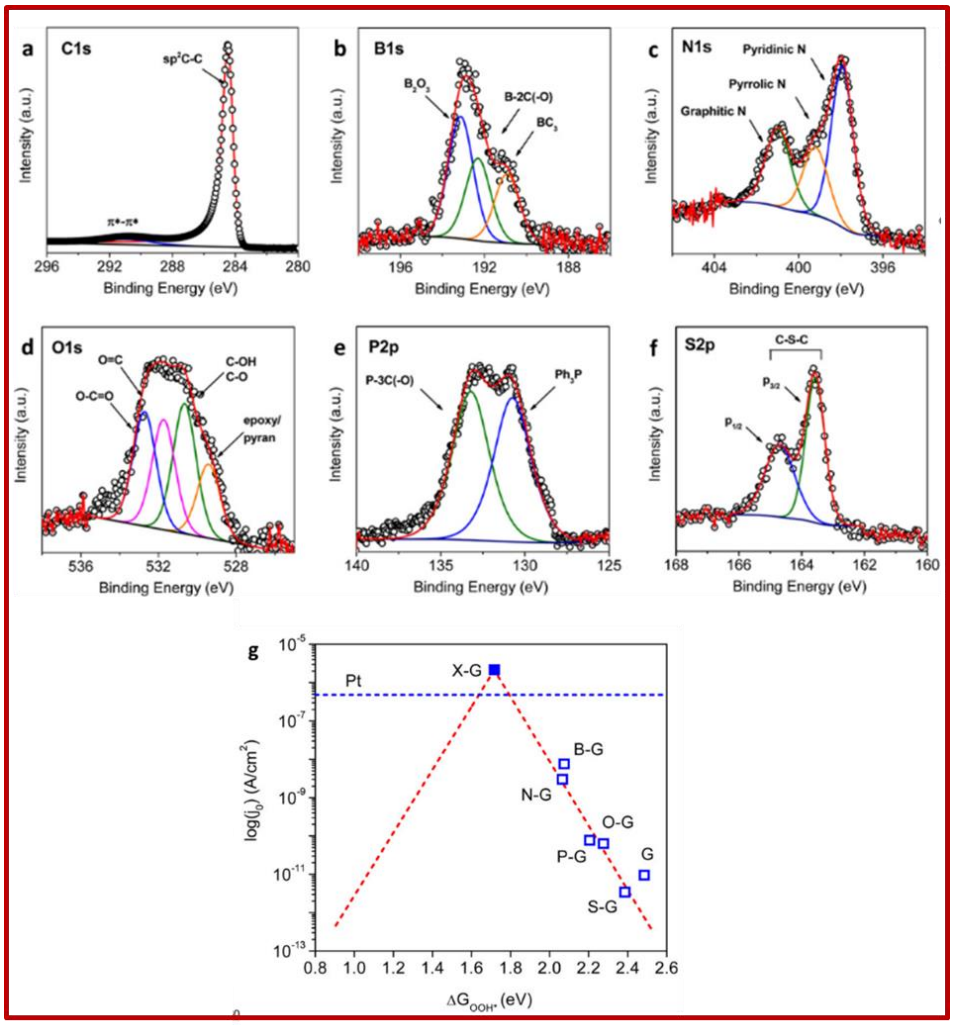

Figure 10. Left panels: High-resolution XPS spectra of different heteroatoms in doped graphene layers: (**a**) graphite. The main peak is due to sp^2 C–C bonds, the lower intensity peak is due to the π plasmon; (**b**) B-graphene with contributions of B_2O_3 (blue), B–2C–O (green), BC_3 (yellow); (**c**) N-graphene with graphitic (green), pyrrolic (yellow) and pyridinic (blue) contributions; (**d**) O-graphene with O-C=O (blue), O=C (pink). C–OH and C–O (green) and epoxyl pyran (yellow) contributions; (**e**) P-graphene with P–3C(–O) (green) and Ph_3P (blue) contributions; (**f**) S-graphene with the S doublet of the C–S–C group. Right panel (**g**): Volcano plot between j_0 theory and ΔGOOH* with charge-transfer coefficient $\alpha = 0.5$ (red dashed line). Blue hollow squares are j_0^{expt} obtained from Tafel plots, and DFT derived ΔG_{OOH^*} for each doped graphene catalyst. Taken with permission from Ref. [52]. Copyright by ACS.

4. Application of Defects and Heteroatoms for Gas Sensing

Since the seminal paper by Schedin et al. [56] several experiments reported the possible use of graphene as a sensing element for the detection of gas-phase molecules, and highly cited review papers have already addressed this topic [57,58].

Two main effects are at the origin of the chemical sensitivity of graphene. These are detectvity/doping, which changes the density of carriers n(t); and scattering, which affects the mobility μ(t).

As a rule of thumb, gas-phase molecules interact more strongly with defects than with pristine graphene but, on the other hand, the higher adsorption energy implies the need for higher temperature annealing, or annealing for longer periods, to regenerate the sensor.

In order to address this issue, studies were performed to shown how the density and type of defects are crucial for real sensing applications.

Extrinsic defects and, in particular, charged impurities are expected to affect the gas sensing performance of graphene, too. Charged gas molecules (after doping) should first adsorb and compensate for the oppositely charged defects on graphene, increasing μ(t), and then adsorb on graphene intrinsically, thus decreasing μ(t).

The experimental verification of this was challenging, but finally achieved by Liu et al. [24]. They developed the method to measure the defect-induced gas adsorptions on a graphene transistor, schematised in Figure 11. In panel c of the same figure the graphs shows a small AC voltage (v_g = 1 V 50 Hz) added on the static DC gate voltage (V_g = −10 V). Both n(t) and μ(t) are obtained from the measure of the graphene conductance g.

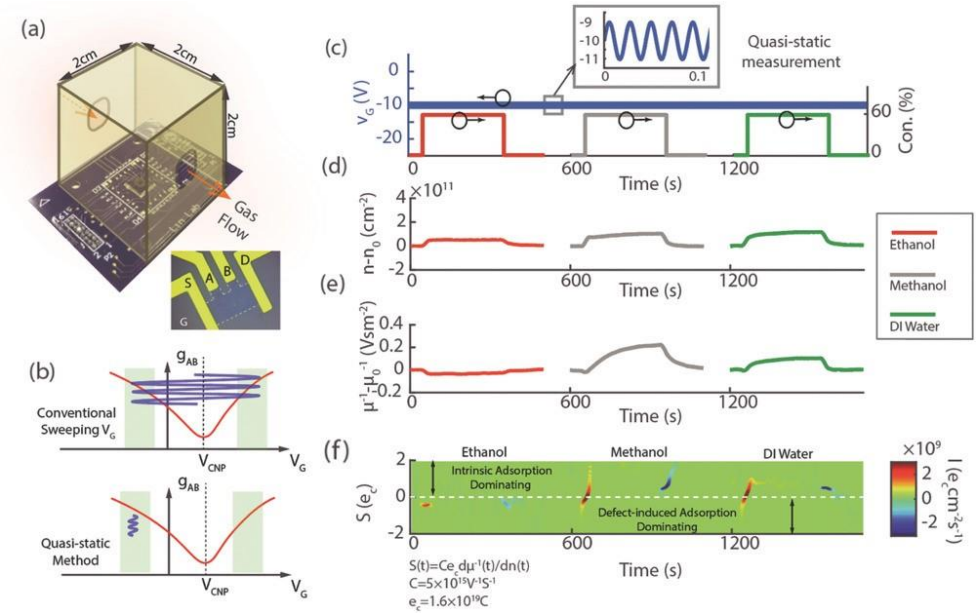

Figure 11. Quasi-static gate voltage method for observing the defect-induced gas adsorptions on a graphene transistor. (**a**) The graphene sensor inside the test chamber with a microscopic photo of the graphene transistor in the inset. (**b**) The schematic diagrams compare the conventional sweeping gate voltage VG and the quasi-static VG method, with the shaded area being the linear regions of the graphene transistor. (**c**) The time series of gate voltage and gas flow; zoom-in view of the gate voltage shown in the inset. (**d**–**f**) Real-time measured results of carrier density n(t), the inverse of field-effect mobility μ^{-1}(t), and the scattering strength S(t) of gas adsorption and desorption on graphene using the quasi-static gate voltage, where $n_0 = 2.0 \times 10^{12}$ cm^{-2}, $\mu_0^{-1} = 4.0$ V s m^{-2} and $e_c = 1.6 \times 10^{-19}$ C is the elementary charge. Figure and caption taken with permission from Ref. [24]. Copyright by Wiley.

This quasistatic method overcomes the limits of the conventional sweeping of V_g around the charge neutrality point (see Figure 11b), which requires spanning a large voltage, thus causing fluctuations of the work function.

Liu et al. observed an increase in the carrier (holes) density after the adsorption of ethanol, methanol or water (all three being p-type doping, see Figure 11d). The inverse of field-effect mobility has a more complex behaviour (Figure 11e) and can increase and decrease depending on the gas types. This indicates that two different adsorption regimes are present: regular and defect-induced gas adsorption. To discriminate between them, Liu et al. introduced the scattering strength $S(t) = Ce_c d\mu^{-1}(t)/dn(t)$, where $C = 20e_c/h = 5 \times 10^{15}$ V^{-1} s^{-1}, which is an intrinsic constant of the graphene FET. In the scattering strength picture, both adsorption regimes have an identical doping effect but an inverted sign: intrinsic adsorption is positive while adsorption on the defects is negative. The plot in Figure 11f reports the scattering strength, emphasizing the transient regions. Adsorption takes place initially at defects (negative S) and then goes on at regular sites

(positive S). The colour scale indicates the charging rate I = dn/dt, which is positive (red) for adsorption and negative (blue) for desorption.

Another experiment worthy of mention is the one by Lee et al. [59], who investigated the sensitivity to NO_2 and NH_3 of commercial graphene in a FET device. Different amounts of defects were created by exposing the sample to oxygen plasma with different power and oxygen flows. During such treatment, oxygen radicals react with graphene, producing sp^3 defects and vacancies, which could be quantified by a careful analysis of the D, G and 2D band intensity in Raman spectra. It was then possible to correlate the relative amount of sp3 defects and vacancies to the sensitivity, thus demonstrating that defect engineering can tune the sensitivity. Vacancies were proved to be essential to activate graphene for the sensing of specific molecules; this is due to the higher adsorption energy at vacancies than at sp3 defects, as evident from the outcome of DFT calculations for different defects (see summary in Table 1).

Table 1. Adsorption energy (in eV) for NO_2 and NH_3 on pristine graphene in the presence of different kinds of sp3 defects, at single vacancies and at N and B-doped sites. Data were taken from Ref. [59] and from [60].

	NO_2	**NH_3**
Pristine graphene	−0.20 [59] −0.48 [60]	−0.11 [59] −0.11 [60]
Epoxide group	−0.21 [59]	−0.16 [59]
Carbonyl group	−0.23 [59]	−0.25 [59]
Ether group	−0.28 [59]	−0.13 [59]
Single vacancy	−2.15 [59]	−1.48 [59]
N-doped	−0.98 [60]	−0.12 [60]
B-doped	−1.37 [60]	−0.50 [60]

From Table 1, we also see that the adsorption energy predicted for B-doped graphene, for both NO_2 and NH_3, is higher than for the pristine graphene and lower than for the defected graphene. This prediction was confirmed experimentally by Chen et al. [61], who found a sensitivity up to ppb and ppm, respectively, for the two gases. Indeed, Figure 12 compares the response of gas sensors based on pristine (Panels A and B) and B-doped (panels C and D) graphene to NO_2 and NH_3. The sensor's active surface is cleaned by exposure to UV light during the experiment. The current measured at different concentrations of NO_2 and NH_3 shows that a minimum concentration of 8 ppb of NO_2 or 20 ppm of NH_3 is needed for pristine graphene; however, when using B-doped graphene, this value decreases to 1 ppb for NO_2 and to 1 ppm for NH_3.

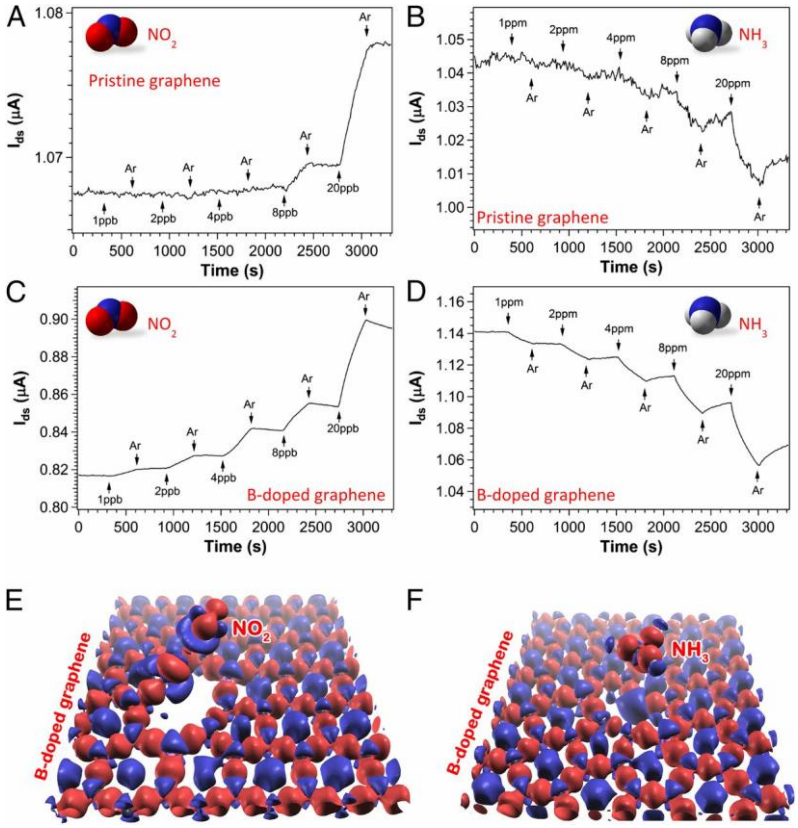

Figure 12. Sensor response of pristine graphene to NO_2 (panel (**A**)) and NH_3 (panel (**B**)) and of B-doped graphene to NO_2 (panel (**C**)) and NH_3 (panel (**D**)). UV illumination was active during all the experiments to maintain a fresh sensor. The difference in charge density with respect to isolated atoms is shown for NO_2 (panel (**E**)) and NH_3 (panel (**F**)) for B-doped graphene. Taken with permission from [61]. Copyright by National Academy of Sciences.

5. Conclusions and Perspectives

In this short review, we have presented a synthesis of the experimental knowledge of the findings on adsorption on graphene in the presence of intrinsic and extrinsic defects. Among all possibilities, we decided to focus on well-defined systems in which a majority defect (either vacancy or non-metal heteroatom) was present. Depending on the system, the adsorption properties under controlled UHV conditions or the catalytic activity in the electrochemical environment are reported. We found that there is a general agreement that defects enhance the reactivity of graphene, making it attractive from the sensoristic and catalytic points of view.

The adsorption energy of the gas of interest must be high enough to allow for a detectable equilibrium coverage at room temperature to be viable for sensoristic application. This requirement excludes the possibility of using pristine unsupported graphene because of the very low physisorption energy of simple gases; it has been demonstrated that the intrinsic response of single-layer graphene to different gases is relatively small if contamination is adequately removed [62]. According to theoretical predictions, experiments indicate that defects can significantly enhance the adsorption energy of gas-phase species with respect to physisorption. However, most theoretical simulations neglect the substrate's role, which is crucial. As we have shown in Section 2, the overall behaviour of defects on supported graphene sheets is influenced not only by the adsorption energy of the gas-phase molecule at the defect but also by the possible formation of chemical bonds between the under-coordinated carbon atoms at the defect sites and the atoms of the substrate. Last but not least, the defect itself may enable intercalation of the gas molecules, leading to the formation of a bond between the gas-phase molecule and the substrate.

A possible alternative is to exploit the use of heteroatoms [57], which saturate the C dangling bonds while preserving the increase in the adsorption energy with respect to pristine graphene, as shown in Section 3. In general, the higher the density of defects, the higher the amount of gas that can adsorb. Unfortunately, however, the introduction of defects affects the mobility of carriers. As shown in Section 4, it is possible to use a defect-based graphene transistor of B-doped graphene-based FET devices to detect several molecules as methanol, water, NO_2 and NH_3.

Based on these conclusions, it is evident that the investigation of intrinsically and extrinsically defected graphene-based material is rapidly developing. Though we limited our review to localised defects and non-metal heteroatoms, we wish to mention two main directions the research is taking forward. The final goal is, of course, to be able to produce innovative materials tailored for the desired scope or application.

For this purpose, one option is the production of graphene layers with more than one dopant [43,45–48]. One example is the simultaneous introduction of B and N atoms inside G [47]. These atoms have a similar size but opposite doping effects, so their simultaneous presence at different concentrations and relative ratios allows for tuning the electronic band structure, bandgap, and chemical-physical properties. When the mixed B-N-C layer is obtained by pyrolytic decomposition of dimethylamine-borane on Pt(111), e.g., a continuous monolayer formed by complementary h-BN and G domains or non-planar hybridised boron, carbonitride layers can form depending on the substrate temperature. Vice versa, stepwise annealing of the layer deposited at RT produces a weakly interacting G layer doped with B or N species.

Another exciting evolution in this field of research is the possibility to insert transition metal (TM) atoms in the graphene lattice, either embedded directly in lattice vacancies (TM-C bonds) or through the interposition of non-metal atoms (e.g., nitrogen with TM-N-C bonds) for a more efficient stabilisation. Indeed, TM containing C-networks are predicted to have interesting electronic and catalytic properties, so to be able to replace currently used catalysts based on precious transition metals. Doping with TM atoms was achieved on porous carbon and graphene-like materials by reacting with suitable precursors [63–65]. These materials were efficient for different catalytic reactions, especially ORR, which was taken as a probe reaction due to its environmental relevance. Much less work is available for more defined systems, such as graphene layers or 1D/2D C-based networks. Though more ideal, these systems allow a much better comprehension of the related phenomena and represent an open challenge in the field.

Author Contributions: All authors contributed equally to literature research, to the writing of the original draft, and to its review, editing and discussion. Funding acquisition: L.V. and L.S. All authors have read and agreed to the published version of the manuscript.

Funding: The article was supported by the following funds, Italian Ministry of Education, University and Research: 2017KFMJ8E_003; Italian Ministry of Education, University and Research: 2017NYPHN8; Fondazione Compagnia di San Paolo: MC-nano.

Institutional Review Board Statement: Not applicable.

Informed Consent Statement: Not applicable.

Data Availability Statement: Data sharing is not applicable to this article.

Conflicts of Interest: The authors declare no conflict of interest.

References

1. Ugeda, M.M.; Brihuega, I.; Guinea, F.; Gómez-Rodríguez, J.M. Missing atom as a source of carbon magnetism. *Phys. Rev. Lett.* **2010**, *104*, 096804. [CrossRef] [PubMed]
2. Meyer, J.C.; Kisielowski, C.; Erni, R.; Rossell, M.D.; Crommie, M.F.; Zettl, A. Direct Imaging of Lattice Atoms and Topological Defects in Graphene Membranes. *Nano Lett.* **2008**, *8*, 3582–3586. [CrossRef] [PubMed]

3. Pašti, I.A.; Jovanović, A.; Dobrota, A.S.; Mentus, S.V.; Johansson, B.; Skorodumova, N.V. Atomic adsorption on graphene with a single vacancy: Systematic DFT study through the periodic table of elements. *Phys. Chem. Chem. Phys.* **2018**, *20*, 858–865. [CrossRef] [PubMed]
4. Sanyal, B.; Eriksson, O.; Jansson, U.; Grennberg, H. Molecular adsorption in graphene with divacancy defects. *Phys. Rev. B* **2009**, *79*, 113409. [CrossRef]
5. Mehmood, F.; Pachter, R.; Lu, W.; Boeckl, J.J. Adsorption and diffusion of oxygen on single-layer graphene with topological defects. *J. Phys. Chem. C* **2013**, *117*, 10366–10374. [CrossRef]
6. Dai, J.; Yuan, J.; Giannozzi, P. Gas adsorption on graphene doped with B, N, Al, and S: A theoretical study. *Appl. Phys. Lett.* **2009**, *95*, 232105. [CrossRef]
7. Zhang, H.P.; Luo, X.G.; Lin, X.Y.; Lu, X.; Leng, Y. Density functional theory calculations of hydrogen adsorption on Ti-, Zn-, Zr-, Al-, and N-doped and intrinsic graphene sheets. *Int. J. Hydrogen Energy* **2013**, *38*, 14269–14275. [CrossRef]
8. Kim, G.; Jhi, S.-H.; Lim, S.; Park, N. Effect of vacancy defects in graphene on metal anchoring and hydrogen adsorption. *Appl. Phys. Lett.* **2009**, *94*, 173102. [CrossRef]
9. Tit, N.; Said, K.; Mahmoud, N.M.; Kouser, S.; Yamani, Z.H. Ab-initio investigation of adsorption of CO and CO_2 molecules on graphene: Role of intrinsic defects on gas sensing. *Appl. Surf. Sci.* **2017**, *394*, 219–230. [CrossRef]
10. Ye, X.L.; Cai, J.; Yang, X.D.; Tang, X.Y.; Zhou, Z.Y.; Tan, Y.Z.; Xie, S.Y.; Zheng, L.S. Quantifying defect-enhanced chemical functionalization of single-layer graphene and its application in supramolecular assembly. *J. Mater. Chem. A* **2017**, *5*, 24257–24262. [CrossRef]
11. Kong, L.; Enders, A.; Rahman, T.S.; Dowben, P.A. Molecular adsorption on graphene. *J. Phys. Condens. Matter* **2014**, *26*, 443001. [CrossRef] [PubMed]
12. Kaur, M.; Kaur, M.; Sharma, V.K. Nitrogen-doped graphene and graphene quantum dots: A review onsynthesis and applications in energy, sensors and environment. *Adv. Colloid Interface Sci.* **2018**, *259*, 44–64. [CrossRef] [PubMed]
13. Ferrighi, L.; Perilli, D.; Selli, D.; Di Valentin, C. Water at the Interface between Defective Graphene and Cu or Pt (111) Surfaces. *ACS Appl. Mater. Interfaces* **2017**, *9*, 29932–29941. [CrossRef] [PubMed]
14. Datteo, M.; Liu, H.; Di Valentin, C. Water on Graphene-Coated TiO2: Role of Atomic Vacancies. *ACS Appl. Mater. Interfaces* **2018**, *10*, 5793–5804. [CrossRef] [PubMed]
15. Ugeda, M.M.; Fernández-Torre, D.; Brihuega, I.; Pou, P.; Martínez-Galera, A.J.; Pérez, R.; Gómez-Rodríguez, J.M. Point defects on graphene on metals. *Phys. Rev. Lett.* **2011**, *107*, 116803. [CrossRef] [PubMed]
16. Ugeda, M.M.; Brihuega, I.; Hiebel, F.; Mallet, P.; Veuillen, J.-Y.; Gómez-Rodríguez, J.M.; Ynduráin, F. Electronic and structural characterization of divacancies in irradiated graphene. *Phys. Rev. B* **2012**, *85*, 121402. [CrossRef]
17. Gawlik, G.; Ciepielewski, P.; Baranowski, J.M. Study of implantation defects in CVD graphene by optical and electrical methods. *Appl. Sci.* **2019**, *9*, 544. [CrossRef]
18. Lehtinen, O.; Kotakoski, J.; Krasheninnikov, A.V.; Tolvanen, A.; Nordlund, K.; Keinonen, J. Effects of ion bombardment on a two-dimensional target: Atomistic simulations of graphene irradiation. *Phys. Rev. B* **2010**, *81*, 153401. [CrossRef]
19. Li, T.; Yarmoff, J.A. Defect-induced oxygen adsorption on graphene films. *Surf. Sci.* **2018**, *675*, 70–77. [CrossRef]
20. Celasco, E.; Carraro, G.; Lusuan, A.; Smerieri, M.; Pal, J.; Rocca, M.; Savio, L.; Vattuone, L. CO chemisorption at vacancies of supported graphene films: A candidate for a sensor? *Phys. Chem. Chem. Phys.* **2016**, *18*, 18692–18696. [CrossRef]
21. Carraro, G.; Celasco, E.; Smerieri, M.; Savio, L.; Bracco, G.; Rocca, M.; Vattuone, L. Chemisorption of CO on N-doped graphene on Ni(111). *Appl. Surf. Sci.* **2018**, *428*, 775–780. [CrossRef]
22. Kolesov, E.A.; Tivanov, M.S.; Korolik, O.V.; Kataev, E.Y.; Xiao, F.; Kapitanova, O.O.; Cho, H.D.; Kang, T.W.; Panin, G.N. Atmospheric adsorption on pristine and nitrogen-doped graphene: Doping-dependent, spatially selective. *J. Phys. D Appl. Phys.* **2020**, *53*, 045302. [CrossRef]
23. Bueno, R.A.; Martínez, J.I.; Luccas, R.F.; del Árbol, N.R.; Munuera, C.; Palacio, I.; Palomares, F.J.; Lauwaet, K.; Thakur, S.; Baranowski, J.M.; et al. Highly selective covalent organic functionalization of epitaxial graphene. *Nat. Commun.* **2017**, *8*, 15306. [CrossRef] [PubMed]
24. Liu, Y.; Liu, H.; Chu, Y.; Cui, Y.; Hayasaka, T.; Dasaka, V.; Nguyen, L.; Lin, L. Defect-Induced Gas Adsorption on Graphene Transistors. *Adv. Mater. Interfaces* **2018**, *5*, 1701640. [CrossRef]
25. Banhart, F.; Kotakoski, J.; Krasheninnikov, A.V. Structural Defects in Graphene. *ACS Nano* **2011**, *5*, 26–41. [CrossRef]
26. Costa, S.D.; Weis, J.E.; Frank, O.; Fridrichová, M.; Bastl, Z.; Kalbac, M. Do defects enhance fluorination of graphene? *RSC Adv.* **2016**, *6*, 81471–81476. [CrossRef]
27. Wu, Q.; Wu, Y.; Hao, Y.; Geng, J.; Charlton, M.; Chen, S.; Ren, Y.; Ji, H.; Li, H.; Boukhvalov, D.W.; et al. Selective surface functionalization at regions of high local curvature in graphene. *Chem. Commun.* **2013**, *49*, 677–679. [CrossRef]
28. Englert, J.M.; Dotzer, C.; Yang, G.; Schmid, M.; Papp, C.; Gottfried, J.M.; Steinrück, H.P.; Spiecker, E.; Hauke, F.; Hirsch, A. Covalent bulk functionalization of graphene. *Nat. Chem.* **2011**, *3*, 279–286. [CrossRef] [PubMed]
29. Perilli, D.; Fiori, S.; Panighel, M.; Liu, H.; Cepek, C.; Peressi, M.; Comelli, G.; Africh, C.; Di Valentin, C. Mechanism of CO Intercalation through the Graphene/Ni(111) Interface and Effect of Doping. *J. Phys. Chem. Lett.* **2020**, *11*, 8887–8892. [CrossRef] [PubMed]
30. Politano, A.; Marino, A.R.; Formoso, V.; Chiarello, G. Water adsorption on graphene/Pt(111) at room temperature: A vibrational investigation. *AIP Adv.* **2011**, *1*, 042130. [CrossRef]

31. Feng, X.; Maier, S.; Salmeron, M. Water splits epitaxial graphene and intercalates. *J. Am. Chem. Soc.* **2012**, *134*, 5662–5668. [CrossRef]
32. Davì, R.; Carraro, G.; Stojkovska, M.; Smerieri, M.; Savio, L.; Lewandowski, M.; Gallet, J.-J.; Bournel, F.; Rocca, M.; Vattuone, L. Graphene growth on Ni (1 1 1) by CO exposure at near ambient pressure. *Chem. Phys. Lett.* **2021**, *774*, 138596. [CrossRef]
33. Matsoso, B.J.; Ranganathan, K.; Mutuma, B.K.; Lerotholi, T.; Jones, G.; Coville, N.J. Time-dependent evolution of the nitrogen configurations in N-doped graphene films. *RSC Adv.* **2016**, *6*, 106914–106920. [CrossRef]
34. Georgakilas, V.; Otyepka, M.; Bourlinos, A.B.; Chandra, V.; Kim, N.; Kemp, K.C.; Hobza, P.; Zboril, R.; Kim, K.S. Functionalization of Graphene: Covalent and Non-Covalent Approaches, Derivatives and Applications. *Chem. Rev.* **2012**, *112*, 6156–6214. [CrossRef] [PubMed]
35. Willke, P.; Amani, J.A.; Sinterhauf, A.; Thakur, S.; Kotzott, T.; Druga, T.; Weikert, S.; Maiti, K.; Hofsäss, H.; Wenderoth, M. Doping of Graphene by Low-Energy Ion Beam Implantation: Structural, Electronic, and Transport Properties. *Nano Lett.* **2015**, *15*, 5110–5115. [CrossRef] [PubMed]
36. Fiori, S.; Perilli, D.; Panighel, M.; Cepek, C.; Ugolotti, A.; Sala, A.; Liu, H.; Comelli, G.; Di Valentin, C.; Africh, C. "Inside out" growth method for high-quality nitrogen-doped graphene. *Carbon* **2021**, *171*, 704–710. [CrossRef]
37. Zhang, C.; Fu, L.; Liu, N.; Liu, M.; Wang, Y.; Liu, Z. Synthesis of nitrogen-doped graphene using embedded carbon and nitrogen sources. *Adv. Mater.* **2011**, *23*, 1020–1024. [CrossRef] [PubMed]
38. Panchakarla, L.S.; Subrahmanyam, K.S.; Saha, S.K.; Govindaraj, A.; Krishnamurthy, H.R.; Waghmare, U.V.; Rao, C.N.R.R. Synthesis, structure, and properties of boron- and nitrogen-doped graphene. *Adv. Mater.* **2009**, *560012*, 4726–4730. [CrossRef]
39. Wang, Y.; Shao, Y.; Matson, D.W.; Li, J.; Lin, Y. Nitrogen-Doped Graphene and Its Biosensing. *ACS Nano* **2010**, *4*, 1790–1798. [CrossRef] [PubMed]
40. Wisitsoraat, A.; Phokaratkul, D.; Maturos, T.; Jaruwongrangsee, K.; Tuantranont, A. Synthesis and characterization of nitrogen-doped 3D graphene foam prepared by inductively-coupled plasma-assisted chemical vapor deposition. In Proceedings of the 2015 IEEE 15th International Conference on Nanotechnology (IEEE-NANO), Rome, Italy, 27–30 July 2015; IEEE: Piscataway, NJ, USA, 2016; pp. 89–92. [CrossRef]
41. Wang, R.; Wang, Y.; Xu, C.; Sun, J.; Gao, L. Facile one-step hydrazine-assisted solvothermal synthesis of nitrogen-doped reduced graphene oxide: Reduction effect and mechanisms. *RSC Adv.* **2013**, *3*, 1194–1200. [CrossRef]
42. Sun, L.; Wang, L.; Tian, C.; Tan, T.; Xie, Y.; Shi, K.; Li, M.; Fu, H. Nitrogen-doped graphene with high nitrogen level via a one-step hydrothermal reaction of graphene oxide with urea for superior capacitive energy storage. *RSC Adv.* **2012**, *2*, 4498. [CrossRef]
43. Wang, T.; Wang, L.-X.; Wu, D.-L.; Xia, W.; Jia, D.-Z. Interaction between Nitrogen and Sulfur in Co-Doped Graphene and Synergetic Effect in Supercapacitor. *Sci. Rep.* **2015**, *5*, 9591. [CrossRef] [PubMed]
44. Liu, H.; Liu, Y.; Zhu, D. Chemical doping of graphene. *J. Mater. Chem.* **2011**, *21*, 3335. [CrossRef]
45. Rao, C.N.R.; Gopalakrishnan, K.; Govindaraj, A. Synthesis, properties and applications of graphene doped with boron, nitrogen and other elements. *Nano Today* **2014**, *9*, 324–343. [CrossRef]
46. Wen, Y.; Rufford, T.E.; Hulicova-Jurcakova, D.; Wang, L. Nitrogen and Phosphorous Co-Doped Graphene Monolith for Supercapacitors. *ChemSusChem* **2016**, *9*, 513–520. [CrossRef] [PubMed]
47. Nappini, S.; Píš, I.; Carraro, G.; Celasco, E.; Smerieri, M.; Savio, L.; Magnano, E.; Bondino, F. On-surface synthesis of different boron–nitrogen–carbon heterostructures from dimethylamine borane. *Carbon* **2017**, *120*, 185–193. [CrossRef]
48. Ai, W.; Luo, Z.; Jiang, J.; Zhu, J.; Du, Z.; Fan, Z.; Xie, L.; Zhang, H.; Huang, W.; Yu, T. Nitrogen and sulfur codoped graphene: Multifunctional electrode materials for high-performance LI-ion batteries and oxygen reduction reaction. *Adv. Mater.* **2014**, *26*, 6186–6192. [CrossRef] [PubMed]
49. Ullah, S.; Shi, Q.; Zhou, J.; Yang, X.; Ta, H.Q.; Hasan, M.; Ahmad, N.M.; Fu, L.; Bachmatiuk, A.; Rümmeli, M.H. Advances and Trends in Chemically Doped Graphene. *Adv. Mater. Interfaces* **2020**, *7*, 2000999. [CrossRef]
50. Figueras, M.; Villar-Garcia, I.J.; Vines, F.; Sousa, C.; De La Pena O'Shea, V.A.; Illas, F. Correcting Flaws in the Assignment of Nitrogen Chemical Environments in N-Doped Graphene. *J. Phys. Chem. C* **2019**, *123*, 11319–11327. [CrossRef]
51. Lai, L.; Potts, J.R.; Zhan, D.; Wang, L.; Poh, C.K.; Tang, C.; Gong, H.; Shen, Z.; Lin, J.; Ruoff, R.S. Exploration of the active center structure of nitrogen-doped graphene-based catalysts for oxygen reduction reaction. *Energy Environ. Sci.* **2012**, *5*, 7936–7942. [CrossRef]
52. Jiao, Y.; Zheng, Y.; Jaroniec, M.; Qiao, S.Z. Origin of the Electrocatalytic Oxygen Reduction Activity of Graphene-Based Catalysts: A Roadmap to Achieve the Best Performance. *J. Am. Chem. Soc.* **2014**, *136*, 4394–4403. [CrossRef] [PubMed]
53. Zhang, H.; Gu, Q.Q.; Zhou, Y.W.; Liu, S.Q.; Liu, W.X.; Luo, L.; Meng, Z. Da Direct Z-scheme photocatalytic removal of ammonia via the narrow band gap MoS2/N-doped graphene hybrid catalyst upon near-infrared irradiation. *Appl. Surf. Sci.* **2020**, *504*, 144065. [CrossRef]
54. Guo, D.; Shibuya, R.; Akiba, C.; Saji, S.; Kondo, T.; Nakamura, J. Active sites of nitrogen-doped carbon materials for oxygen reduction reaction clarified using model catalysts. *Science* **2016**, *351*, 361–365. [CrossRef] [PubMed]
55. Zoppellaro, G.; Bakandritsos, A.; Tuček, J.; Błoński, P.; Susi, T.; Lazar, P.; Bad'ura, Z.; Steklý, T.; Opletalová, A.; Otyepka, M.; et al. Microwave Energy Drives "On–Off–On" Spin-Switch Behavior in Nitrogen-Doped Graphene. *Adv. Mater.* **2019**, *31*, 1902587. [CrossRef] [PubMed]
56. Schedin, F.; Geim, A.K.; Morozov, S.V.; Hill, E.W.; Blake, P.; Katsnelson, M.I.; Novoselov, K.S. Detection of individual gas molecules adsorbed on graphene. *Nat. Mater.* **2007**, *6*, 652–655. [CrossRef] [PubMed]

57. Yuan, W.; Shi, G. Graphene-based gas sensors. *J. Mater. Chem. A* **2013**, *1*, 10078–10091. [CrossRef]
58. Varghese, S.S.; Lonkar, S.; Singh, K.K.; Swaminathan, S.; Abdala, A. Recent advances in graphene based gas sensors. *Sens. Actuators B Chem.* **2015**, *218*, 160–183. [CrossRef]
59. Lee, G.; Yang, G.; Cho, A.; Han, J.W.; Kim, J. Defect-engineered graphene chemical sensors with ultrahigh sensitivity. *Phys. Chem. Chem. Phys.* **2016**, *18*, 14198–14204. [CrossRef]
60. Zhang, Y.-H.; Chen, Y.; Zhou, K.-G.; Liu, C.; Zeng, J.; Zhang, H.; Peng, Y. Improving gas sensing properties of graphene by introducing dopants and defects: A first-principles study. *Nanotechnology* **2009**, *20*, 185504. [CrossRef] [PubMed]
61. Lv, R.; Chen, G.; Li, Q.; McCreary, A.; Botello-Méndez, A.; Morozov, S.V.; Liang, L.; Declerck, X.; Perea-López, N.; Cullen, D.A.; et al. Ultrasensitive gas detection of large-area boron-doped graphene. *Proc. Natl. Acad. Sci. USA* **2015**, *112*, 14527–14532. [CrossRef] [PubMed]
62. Dan, Y.; Lu, Y.; Kybert, N.J.; Luo, Z.; Johnson, A.T.C. Intrinsic Response of Graphene Vapor Sensors. *Nano Lett.* **2009**, *9*, 1472–1475. [CrossRef] [PubMed]
63. Lee, S.; Lee, Y.W.; Kwak, D.H.; Lee, J.Y.; Han, S.B.; Sohn, J.I.; Park, K.W. Three-dimensional porous metal–nitrogen doped carbon nanostructure as a superior non-precious electrocatalyst in oxygen reduction reaction. *J. Ind. Eng. Chem.* **2016**, *43*, 170–176. [CrossRef]
64. Wu, G.; Santandreu, A.; Kellogg, W.; Gupta, S.; Ogoke, O.; Zhang, H.; Wang, H.L.; Dai, L. Carbon nanocomposite catalysts for oxygen reduction and evolution reactions: From nitrogen doping to transition-metal addition. *Nano Energy* **2016**, *29*, 83–110. [CrossRef]
65. Chen, Y.; Ji, S.; Wang, Y.; Dong, J.; Chen, W.; Li, Z.; Shen, R.; Zheng, L.; Zhuang, Z.; Wang, D.; et al. Isolated Single Iron Atoms Anchored on N-Doped Porous Carbon as an Efficient Electrocatalyst for the Oxygen Reduction Reaction. *Angew. Chem.* **2017**, *129*, 7041–7045. [CrossRef]